
Audiomagnetotelluric investigation of seawater intrusion using 2-D inversion of invariant impedances

VIOLETA LUJÁN and JOSÉ MANUEL ROMO |*|

División de Ciencias de la Tierra, Centro de Investigación Científica y de Educación Superior de Ensenada, (CICESE)
Carretera Ensenada-Tijuana 3918, frac. Zona Playitas. Ensenada, B.C., 22860, México

* corresponding author E-mail: jromo@cicese.mx

| ABSTRACT |

An audio-magnetotelluric survey was conducted to estimate the extension of the seawater intrusion in a coastal aquifer, in Ensenada, Baja California, México. The survey consisted of 134 closely spaced sites along three profiles 5 to 6 km long. The four elements of the impedance tensor were measured at every observation site and used to estimate the series and parallel (s-p) invariant impedances. 2-D resistivity models were obtained along each profile using a Gauss-Newton regularized inversion process. The seawater intrusion is clearly shown in the resulting models as highly conductive anomalies. In some places, the resistivity models show the bedrock and the basement faults in good agreement with structures interpreted from gravity and magnetic modeling. Based on the information provided by the resistivity models and using the available hydrogeologic information, we used Archie's law in an attempt to gain insights about porosity and TDS distributions in the aquifer. Porosity values between 15 and 25% near the surface reasonably predict the TDS values observed in several shallow wells in the area. TDS values range from 40 g/l typical for seawater to 1 g/l in the eastern edge of the basin, 4 km away from the coastline. The best conditions were found in Profile 2, where the resistivity model predicts TDS values close to 1 g/l below 100 m depth at sites located further than 1 km from the coast. The above results show that s-p invariant impedances produced geologically plausible resistivity models. Hence, they might be a convenient set of magnetotelluric responses to be used for routine 2-D inversion of AMT data.

KEYWORDS | Seawater intrusion. Magnetotellurics. Baja California. México.

INTRODUCTION

Maneadero Valley is a small geological basin located south of the city of Ensenada, between latitudes 31° 41' and 31° 45' N, and 116° 34' to 116° 38' W longitude, in Baja California, México (Fig. 1). The extensive extraction of groundwater from an aquifer contained within the

alluvial deposits that fill the basin has caused the intrusion of seawater and the subsequent degradation of the fresh-water quality. There is a need to study the geological and hydrogeological situation in the basin as it represents the source of water supply for extensive agricultural activity and for human use in Ensenada. Depths to bedrock and information about the geometry and structure of the basin

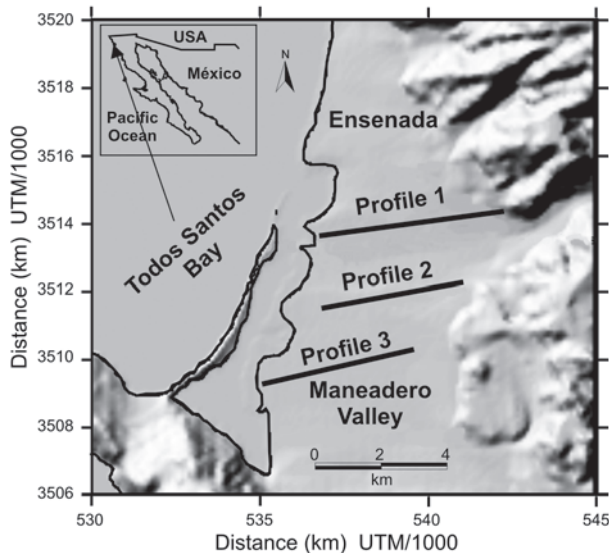


FIGURE 1 | Study area in northern Baja California, México, showing the location of three AMT profiles in Maneadero Valley, south of Ensenada.

have been derived from gravity and magnetic geophysical surveys (Cruz-Falcón, 1986; Fabriol et al., 1982; Pérez-Flores et al., 2004; Vázquez, 1980). However, there is insufficient information about the physical properties of the aquifer (Sarmiento-López, 1996; Vega-Aguilar, 1989). A particularly useful property is electrical resistivity, as it depends on porosity, fluid content and pore-fluid resistivity which is directly related to the salt content of the water. Hence, we conducted an electromagnetic survey using audiomagnetotellurics (AMT) to investigate the subsurface resistivity distribution. Besides contributing to advancing the knowledge of the physical properties of the Maneadero aquifer, the work also illustrates the performance of a recently proposed set of magnetotelluric response functions (Romo et al., 2005). As discussed below, these new response functions have some useful advantages that make them suitable for a regular use in AMT interpretation practice.

GEOLOGICAL SETTING

The valley of Maneadero is located in a small basin filled with sediments produced by the erosion of volcanic and granitic rocks outcropping in the surroundings. The origin of this structure is associated with a period of intense erosion and uplift at the end of the Cretaceous, when a rapid uplift of the peninsular block provoked the erosion of highlands and the formation of deep creeks which transported considerable amounts of sediment to the Pacific coast (Gastil et al., 1975). The basin is a semi-graben structure limited to the south by Agua Blanca fault, a seismically active regional fault (Pérez-Flores et al., 2004; Suárez-Vidal et al., 1991).

The basement rocks consist of a volcanic and volcanoclastic sequence, largely intruded by granodioritic rocks of the Peninsular Ranges Batholith (PRB), which was formed during a regional magmatic accretion event that occurred along the Baja California Peninsula in Cretaceous time. Basement rocks outcrop in the hills to the east of the valley, forming the eastern edge of the basin. The basement deepens westward to a depth of 900 m close to the coast and 1650 m offshore in Todos Santos Bay (Pérez-Flores et al., 2004). At the bottom of the basin, rocks of the Group Rosario overlay Alisitos basement discordantly. Group Rosario consists of poorly consolidated marine sediments (Abbott et al., 1993; Suárez-Vidal, 2006), these rocks outcrop south of Maneadero valley, in Punta Banda peninsula and north of Ensenada city. Cruz-Castillo and Delgado-Argote (2000) describe the intermediate member of Group Rosario as a medium to fine grained sandstone inter-stratified with shale, mudstone, sand and clay, as well as with conglomerates, overlaid by an upper member consisting of conglomerate with pebbles between 2 and 20 cm in diameter, with a size of 10 cm prevailing. Overlaying Group Rosario discordantly, there is a sequence of Quaternary alluvial sediments consisting of granular material with good permeability represented by bodies of conglomerates, medium to fine grained sands and clays which were deposited at the bottom of the streams as well as in the low lands surrounding topographic elevations.

The currently exploited aquifer is contained in these alluvial deposits; it is an unconfined aquifer, hydraulically connected with the Pacific Ocean. The volume of water extraction has been estimated to be $25.7 \times 10^6 \text{ m}^3/\text{year}$, while the aquifer recharge is about $20.8 \times 10^6 \text{ m}^3/\text{year}$ (Daessle et al., 2004). This negative balance, sustained for several years, provoked a severe sea-water intrusion that is causing a gradual deterioration of the water quality in the aquifer. Daessle et al. (2004) analyzed TDS (total dissolved solids) in water from 25 wells distributed within the valley. They concluded that sea-water invasion has progressed particularly in the central part and in the coastal area where values as high as 9.6 g/l occur. The geophysical information provided by this work helps to estimate the extension and magnitude of the intrusion in places where well information is not available.

METHODOLOGY

Geophysical methods designed to investigate the electrical resistivity of the subsurface are widely used in groundwater investigations because conduction of electricity in the subsurface rocks depends mainly on their water content, water salinity and permeability. There are several geophysical methods sensitive to the subsurface

electrical resistivity. Some of them inject direct current in the ground and measure the voltages produced at the surface (Kirsch, 2006; Wilson et al., 2006) and some others induce electrical fields that spread underground and produce magnetic fields detectable at the surface (Giroux et al., 1997; Meju et al., 1999; Ritz et al., 1997). In this work, we used audio-magnetotellurics (AMT): a technique that uses natural electromagnetic fields produced mainly by electric storms around the world which propagate as electromagnetic plane-waves in the ground (McNeill, 1990). The resistivity distribution in the ground is estimated from the horizontal components of the electric and magnetic fields measured at the surface. The temporal variation of the EM fields is registered for a frequency band between 10 Hz to 100 kHz. At the highest frequencies (750Hz to 100 kHz), the natural signal is extremely weak, thus an external source is used to enhance the signal-to-noise ratio. The artificial source produces plane-waves provided that the transmitting antenna is located in the far-field, i.e., about 3 skin-depths from the measurement site.

In the frequency domain, the relationship between the horizontal components of the electric and magnetic fields is given by

$$\begin{pmatrix} E_x \\ E_y \end{pmatrix} = \begin{pmatrix} Z_{xx} & Z_{xy} \\ Z_{yx} & Z_{yy} \end{pmatrix} \begin{pmatrix} H_x \\ H_y \end{pmatrix},$$

$$\mathbf{E} = \mathbf{Z} \mathbf{H} \quad (1)$$

where \mathbf{Z} is the impedance tensor. The four elements of the tensor contain the information of the ground resistivity distribution.

The elements of the impedance tensor are frequency-dependent complex variables which can be represented, at each AMT site, by apparent resistivity $\rho(\omega)$ and phase $\phi(\omega)$ curves

$$\rho(\omega) = \frac{1}{\omega\mu_0} |\mathbf{Z}(\omega)|^2, \quad (2)$$

and

$$\phi(\omega) = \arctan \left(\frac{\Im m(\mathbf{Z}(\omega))}{\Re e(\mathbf{Z}(\omega))} \right), \quad (3)$$

where μ_0 is the free-space magnetic permeability and ω is the angular frequency.

A common practice consists of interpreting the measured tensor in terms of two-dimensional (2-D) resistivity models, i.e., to assume that the ground resistivity depends on depth and one horizontal direction. In a simple

2-D case, the electrical current flow can be decoupled in two orthogonal systems: along strike and across strike. These directions define the so-called TE (transverse electric) and TM (transverse magnetic) polarization modes. If the coordinate axes are conveniently oriented along the 2-D strike, the diagonal elements of \mathbf{Z} reduce to zero and the off-diagonal terms are the TE and TM impedances. Thus, equation (1) decouples in a pair of independent scalar equations.

A widely used approach to reduce the measured full tensor to an off-diagonal form assumes that \mathbf{Z} is composed of a regional, off-diagonal, 2-D tensor distorted by local 3-D effects (Bahr, 1988, 1991; Groom and Bailey, 1989, 1991). This method has proved very useful in practice whenever the 2-D assumption is supported by the geological situation, i.e., that any 3-D heterogeneity can be considered as local geological noise perturbing a regional 2-D structure.

Another line of work makes no assumption about the Earth's dimensionality. It recognizes that the full tensor completely describes the underground response and uses mathematical transformations in order to find more useful or simpler representations of the response function (e.g., Eggers, 1982; Yee and Paulson, 1987; Romo et al., 2005). These transformation methods preserve all the information contained in the original tensor, i.e., it is always possible to retrieve the original tensor elements by means of an inverse transformation.

In contrast, decomposition methods find an approximate solution minimizing the misfit between a pair of 2-D impedances and the original tensor elements.

In this work, we use the series and parallel (s-p) transformation proposed by Romo et al. (2005). With this application, we intend to further explore the performance of this method in a relatively simple geological situation: an alluvial basin filling up a 2-D semi-graben structure. The lateral influence of the seawater intrusion is also expected as a 2-D anomaly oriented along the semi-graben structure.

The method transforms the four elements of the original tensor into four complex quantities: two impedances and two angular functions,

$$\{Z_{xx}, Z_{xy}, Z_{yx}, Z_{yy}\} \Leftrightarrow \{Z_S, Z_P, \bar{\theta}, \Delta\theta\}, \quad (4)$$

Romo et al. (2005) show that the series Z_S and parallel Z_P impedances are complementary to each other in the sense that Z_S is more sensitive to the galvanic effect produced by accumulation of electric charge across resistivity interfaces, while Z_P is more sensitive to the inductive effect of electric current traveling along conductive bodies. This

property of the s-p impedances resembles the sensitivity to inductive and galvanic effects of the TE-TM modes in a 2-D geometry. Conversely, the s-p impedances do not depend of the orientation of the measurement coordinate axes, i.e., they are rotation invariant quantities that can be used to obtain models of the ground resistivity distribution with no a-priori assumptions about the geometry or direction of the geological structures.

Z_S and Z_P are easily estimated from the original tensor elements by

$$Z_S = \left(\frac{Z_{xx}^2 + Z_{xy}^2 + Z_{yx}^2 + Z_{yy}^2}{2} \right)^{1/2} \quad \text{and}$$

$$Z_P = \sqrt{2} \frac{Z_{yx}Z_{xy} - Z_{xx}Z_{yy}}{(Z_{xx}^2 + Z_{xy}^2 + Z_{yx}^2 + Z_{yy}^2)^{1/2}}. \quad (5)$$

Accompanying Z_S and Z_P , the s-p transformation produces two complex angular functions $\Delta\theta$ and $\Delta\bar{\theta}$.

$$\Delta\theta = \arctan \left(\frac{Z_{xx} + Z_{yy}}{Z_{xy} - Z_{yx}} \right) \quad \text{and}$$

$$\bar{\theta} = \frac{1}{2} \arctan \left(\frac{Z_{yy} - Z_{xx}}{Z_{xy} + Z_{yx}} \right). \quad (6)$$

We utilize the real part of the angular difference $\Delta\theta$ as a measure of the tensor skew which is a quantity commonly used in magnetotellurics as an indicator of three-dimensionality. On the other hand, the real part of the angular average $\Delta\bar{\theta}$ reduces to the rotation angle (Romo et al., 2005) which is an estimate of the structural azimuth.

Thus, the s-p transformation synthesizes the full tensor in two impedances and two complex angular functions. This set of four complex functions can be used in an inversion scheme to obtain a resistivity model of the ground. In the general 3-D case the full set is suitable for inversion, as is the original full tensor. In 2-D inversion only Z_S and Z_P are utilized, as the angular functions $\Delta\theta$ and $\Delta\bar{\theta}$ reduce to zero.

AUDIOMAGNETOTELLURIC SURVEY

We occupied a total of 134 AMT sites along three profiles perpendicularly to the coast line (Fig. 1). Observation sites were separated by 100 m for most of the profile length,

with separations increasing to 200 m close to the eastern limit of the basin. At each site, temporal variations of the horizontal components of both electric and magnetic fields were simultaneously measured using the Stratagem EH4 data acquisition system (Geometrics-EMI). The estimated impedance tensor was then transformed into s-p impedances to be used with an inversion algorithm to construct 2-D resistivity models of the subsurface. Fig. 2 presents typical apparent resistivity and phase data observed in some sites along Profile 1. The sites selected give an idea about the behavior of the response curves along the whole profile. The first row shows the traditional TE-TM apparent resistivity and phase curves, while the corresponding s-p curves are shown in the second row. It is evident that s-p apparent resistivity curves are nearly coincident, while some split is observable in the TE-TM curves, particularly in sites 20 and 26. This is an expected attribute of the s-p impedances as they are a kind of average of the tensor elements. On the other hand, TE and TM impedances are extreme values of the off-diagonal tensor elements.

It is worth mentioning that the closeness of the s-p curves to each other somehow implies a loss of lateral resolution, although not as severe as the one involved by using the determinant of the impedance tensor, which is also an invariant quantity. In some way, this is a cost to pay for using rotation invariant quantities. The benefit is that invariant response functions are usually easy to explain by 1-D or 2-D simple models. In contrast, it frequently happens that TE and TM impedances are not equally well fitted by a simple 2-D model; commonly, the TE mode is more difficult to explain. This is because the TE mode exists only in the ideal 2-D case, thus it is hard to find natural situations satisfying such conditions in the whole frequency range of interest.

The third row in Fig. 2 shows histograms of the tensor skew as derived from the real part of $\Delta\theta$. Values larger than $\pm 15^\circ$ are indicative of three-dimensional effects. This is equivalent to a skew > 0.3 , as defined by Vozoff (1991). In most of the sites, we obtain values smaller than this limit, suggesting that no significant three-dimensional effects are occurring along the profile. Site 44 has a very large dispersion but the central value remains close to 10° .

The structural azimuth derived from $\Delta\bar{\theta}$ is shown in the fourth row of Fig. 2, plotted in rose diagrams. The azimuth ranges from 310° to 30° in most sites, implying that structures are oriented almost perpendicular to the profiles (Fig. 1).

2-D INVERSION

Along each profile, the subsurface was represented by a 2-D grid of rectangular cells. The inversion process starts with a homogeneous half-space that is iteratively modified

A

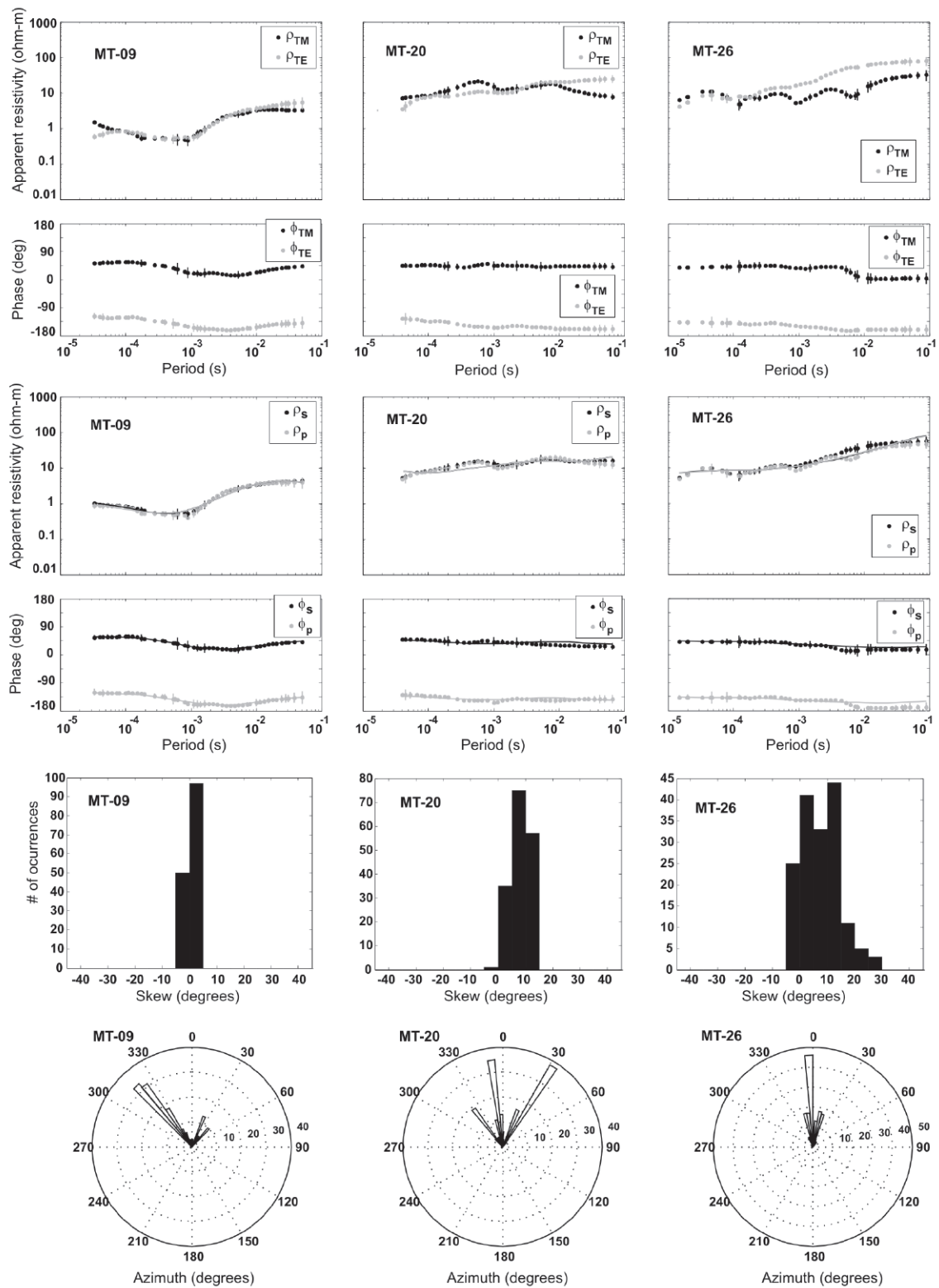


FIGURE 2 | Apparent resistivity and phase at six sites along Profile 1. a) sites 09, 20 and 26; B) sites 35, 38 and 44. TE-TM curves are shown in the first row, while s-p curves are in the second row. The continuous lines in the s-p curves are calculated responses produced by the 2-D resistivity model. The third and fourth rows show histograms for the impedance skewness and azimuth, respectively. (Panel A in page 55 and panel B in page 56).

B

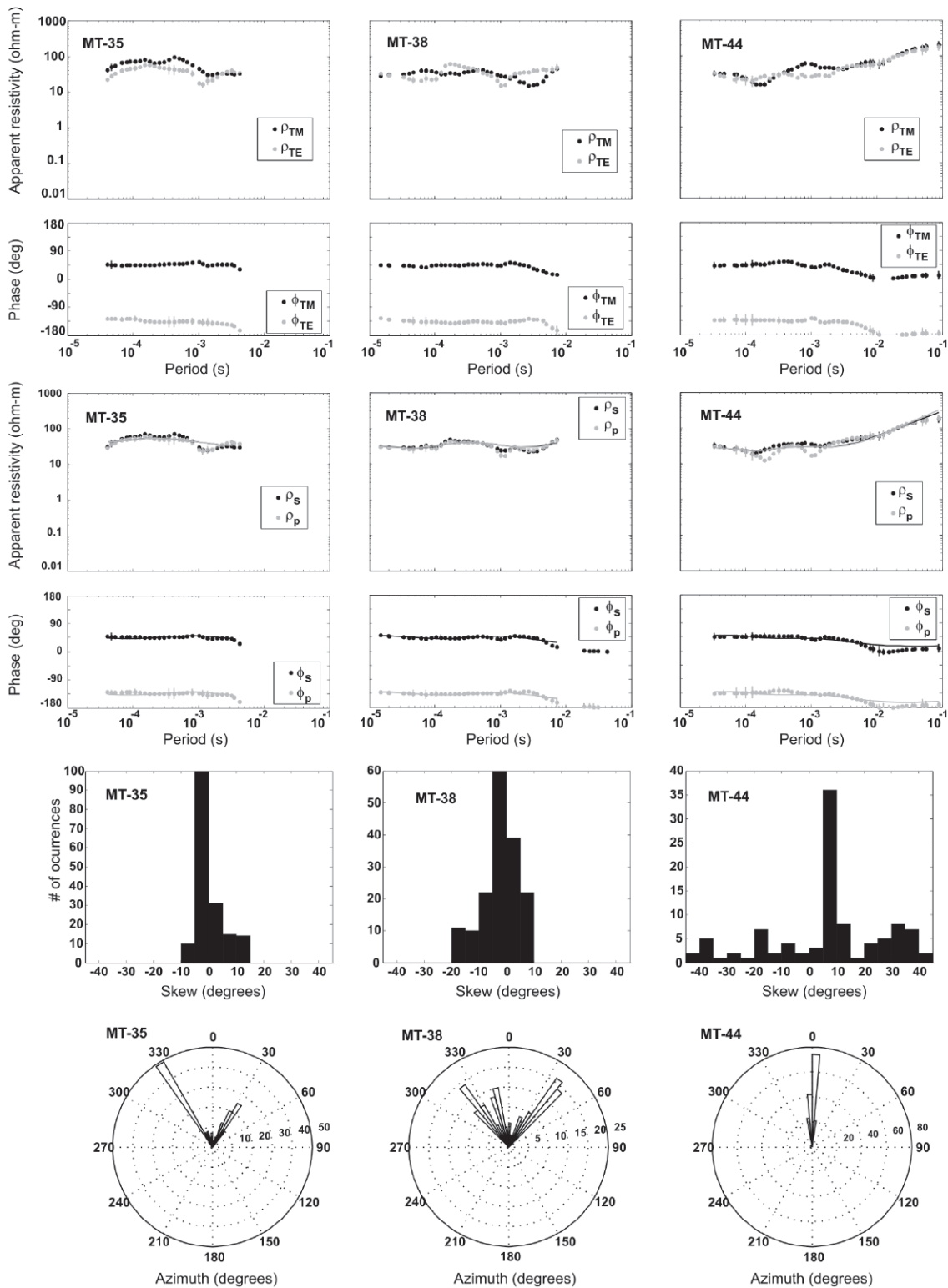


FIGURE 2 | Continuation. See caption in page 55.

by an optimization algorithm in the search for a resistivity distribution capable of reproducing the observed data. Our models have about 50 by 50 cells, with a thickness as small as 2 m close to the surface and increasing logarithmically with depth. The horizontal dimensions of the mesh were designed to accommodate one observed site in each model cell. Starting with a homogeneous model of 100 ohm-m, the inversion is completed when the convergence criteria are fulfilled. In most cases, our solutions converged after 50 or 100 iterations.

We use a regularized 2-D inversion algorithm based on Gauss-Newton optimization, originally written by Rodi and Mackie (2001) and modified to deal with the s-p impedances. The algorithm minimizes the misfit between observed data and model responses in the least square sense. At the same time, the roughness of the model is constrained by minimizing the variation of the model resistivity. The tradeoff between data fitness and model roughness is controlled by the so-called regularization factor τ . We explore several solutions experimenting with different regularization factors. Excessively smooth models have large data misfits, whereas reducing the data misfit too much might result in unacceptably rough models. The solution with the best tradeoff between data fitness and model roughness was chosen using the L curve criteria (Farquharson and Oldenburg, 2004; Hansen, 1992), i.e., the model with the best balance between data misfit and model roughness.

Fig. 3A shows the L curve obtained for Profile 1 after nine experiments with different regularization factors. The L curve shows that RMS ranges from 25 to 28%, for τ varying from 5 to 300, i.e., decreasing τ does not significantly reduce the data misfit. However, for $\tau < 30$ the model roughness increases substantially. Hence, we chose $\tau = 30$ as the best tradeoff between RMS and model roughness. It is worthwhile to mention that the RMS is calculated considering the four response curves at each site (two apparent resistivity and two phase curves).

The corresponding resistivity model is shown in Fig. 3B. The bar graph at the top of the resistivity cross-section shows the misfit obtained at every site. The misfit value ranges from 2 to 10 standard deviations (sd), i.e., 10 to 50%, given a noise floor of 5% for apparent resistivity and 2.5% for phase data.

In order to provide a glimpse of the misfit variation along the whole profile, we plot apparent resistivity and phase curves for the best and the worst fitted sites along the profile as well as pseudosections, i.e., 2-D graphs representing apparent resistivity and phase as a function of horizontal distance and period. Fig. 3C shows pseudosections of observed data and calculated responses. Both responses,

apparent resistivity and phase, are reasonably reproduced by the model in the whole period range. The largest misfit occurs at the longest periods in the phase pseudosections, particularly in the eastern half of the profile. Only the series impedances are shown. The corresponding parallel impedances behave similarly.

The results for Profiles 2 and 3 are shown in Figs. 4 and 5, respectively. In both cases, we experimented with seven different regularization factors, achieving the best tradeoff with $\tau = 30$. For Profile 2, the data fitness is better than 5 sd for most of the sites, but at site 05 it is larger than 10 sd (Fig. 4B) which contributes to increasing the total RMS to 27.8% (5.6 sd). A comparison of observed and calculated pseudosections (Fig. 4C) shows that the observed apparent resistivity is well reproduced by the model, while the calculated phase is rather smoother than the observed data. This is because the observed phase has a larger data dispersion that is not reproduced by the model. For Profile 3, the total RMS is 24.7% (4.9 sd), while the misfit at each individual site is better than 5 sd, as shown in the bar graph (Fig. 5B). Along this profile, the signal to noise ratio during the field operation was lower than in the others. Thus, the observed pseudosections for Profile 3 (Fig. 5C) show a larger dispersion than the one found in Profiles 1 and 2. Consequently, the calculated responses look considerably smoother than the observed ones.

We believe that the obtained resistivity models are consistent images of the underground resistivity distribution in the studied area as they are very well constrained by a large number of closely spaced observation sites. Moreover, they resulted from a systematic exploration of the solution space, as different regularization factors were tested.

RESULTS

Geoelectric interpretation

Fig. 6 summarizes our results for the three profiles in terms of geological structures. The most shallow section in the three resistivity models shows a thin, highly conductive (< 3 ohm-m) layer, about 30 m thick, extending horizontally along their whole length. This is most likely associated with salty soils caused by high evaporation rates. Close to the coastline, this is probably due to seawater evaporation of inundated areas, but toward the east, it is probably related to processes in the vadose zone.

The wedge shaped, highly conductive anomaly (< 3 ohm-m) observed in the western side of Profile 1 is probably due to seawater intrusion. The top of the anomaly deepens eastward as expected for a salt-fresh water transition zone. From 2.5 to 5.5 km of horizontal distance, the resistivity

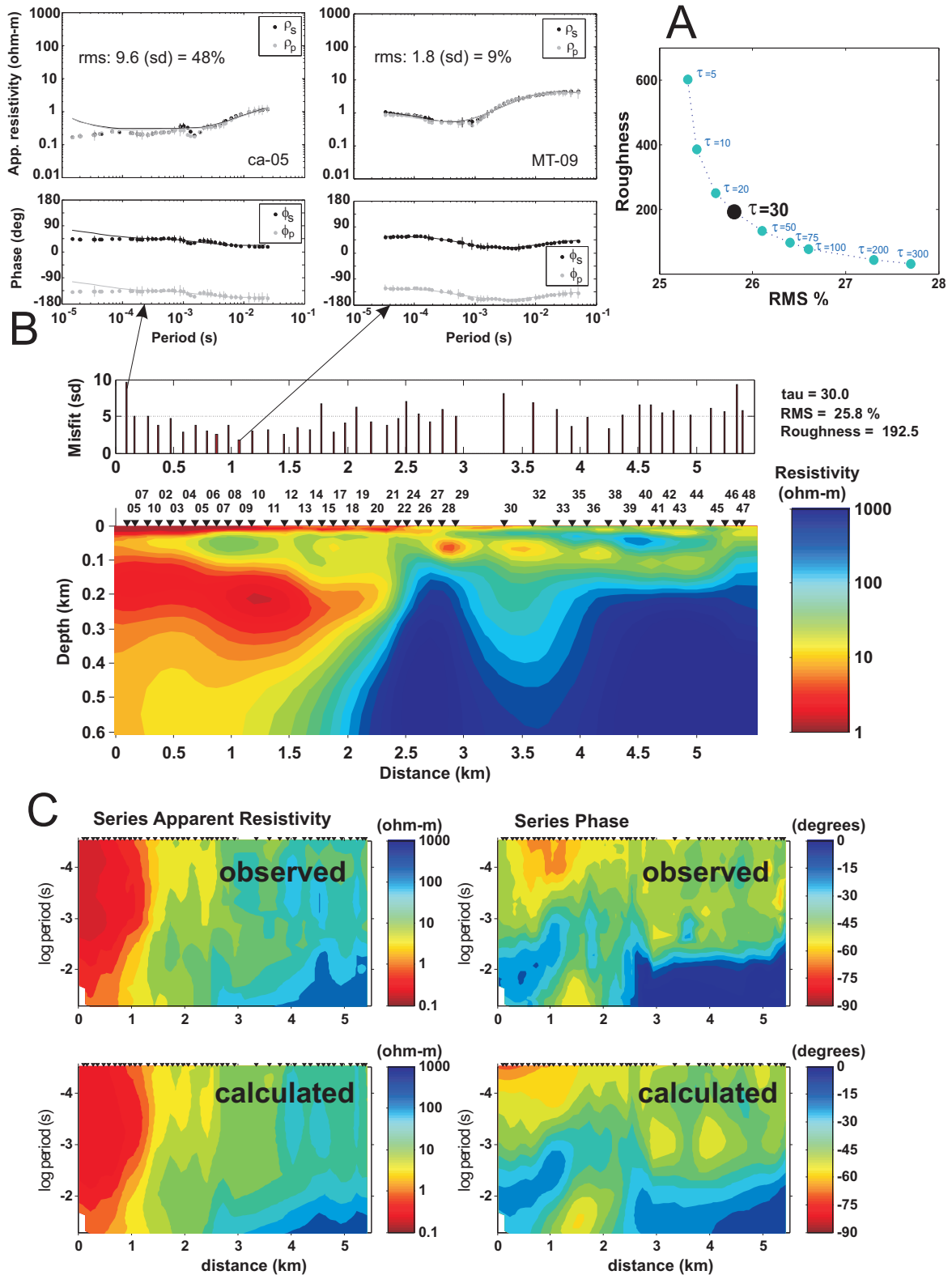


FIGURE 3 | Inversion results for Profile 1. A) L-curve showing the tradeoff between data misfit (RMS) and model roughness. The best tradeoff is for a regularization factor $\tau = 30$. B) 2-D resistivity model. The location of the AMT sites is shown by triangles at the top of the model. In the upper panel, the misfit for each individual site is shown in standard deviation (sd) units, 1 sd corresponds to an error floor of 5%. Apparent resistivity and phase curves are shown for the sites with the best and worst misfits (continuous lines correspond to model responses). C) pseudosections comparing observed and calculated responses for the series apparent resistivity and phase.

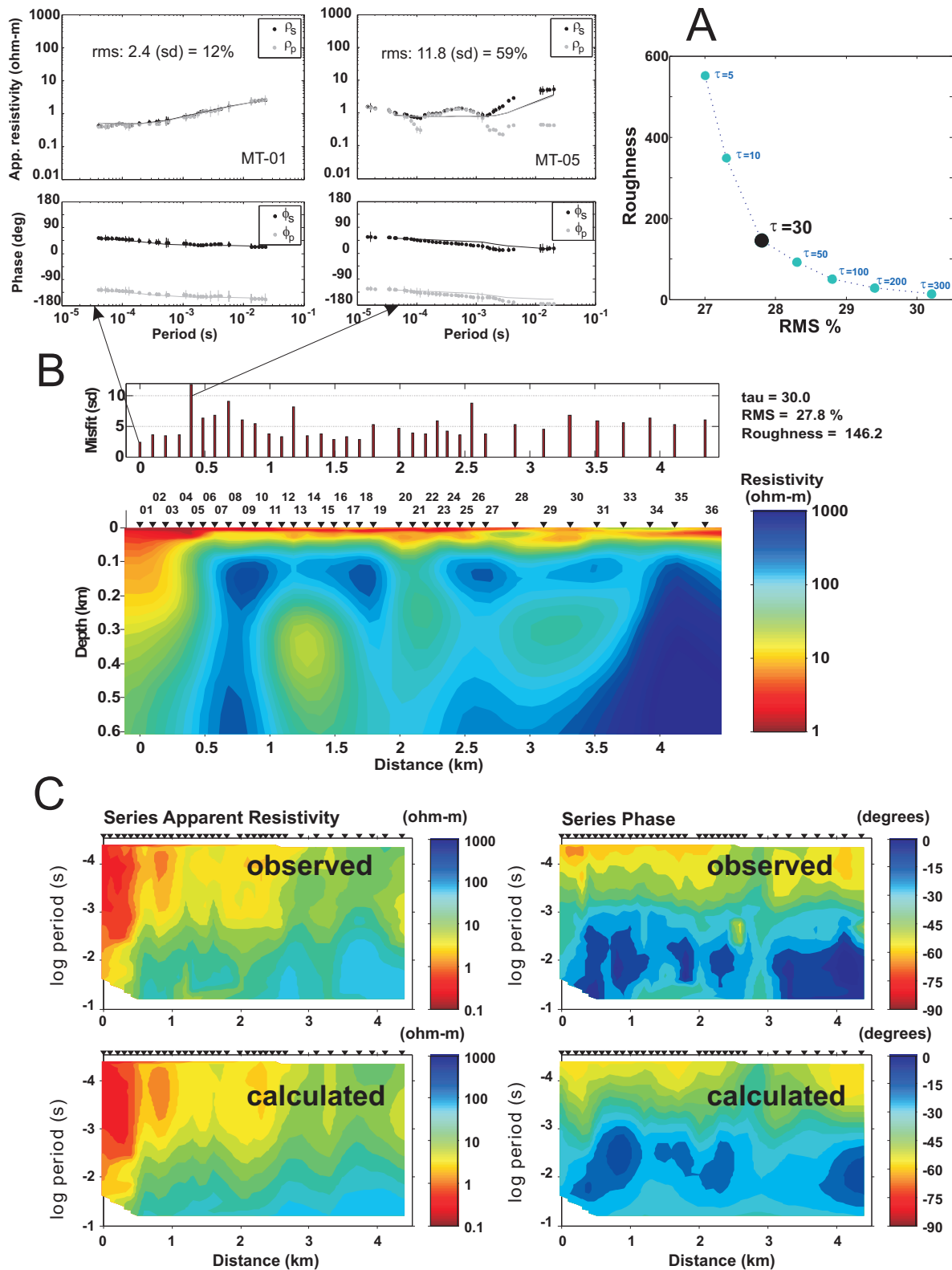


FIGURE 4 | Inversion results for Profile 2. A) L-curve showing the tradeoff between data misfit (RMS) and model roughness. The best tradeoff is for a regularization factor $\tau = 30$. B) 2-D resistivity model. The location of the AMT sites is shown by triangles at the top of the model. In the upper panel, the misfit for each individual site is shown in standard deviation (sd) units, 1 sd corresponds to an error floor of 5%. Apparent resistivity and phase curves are shown for the sites with the best and worst misfits (continuous lines correspond to model responses). C) pseudosections comparing observed and calculated responses for the series apparent resistivity and phase.

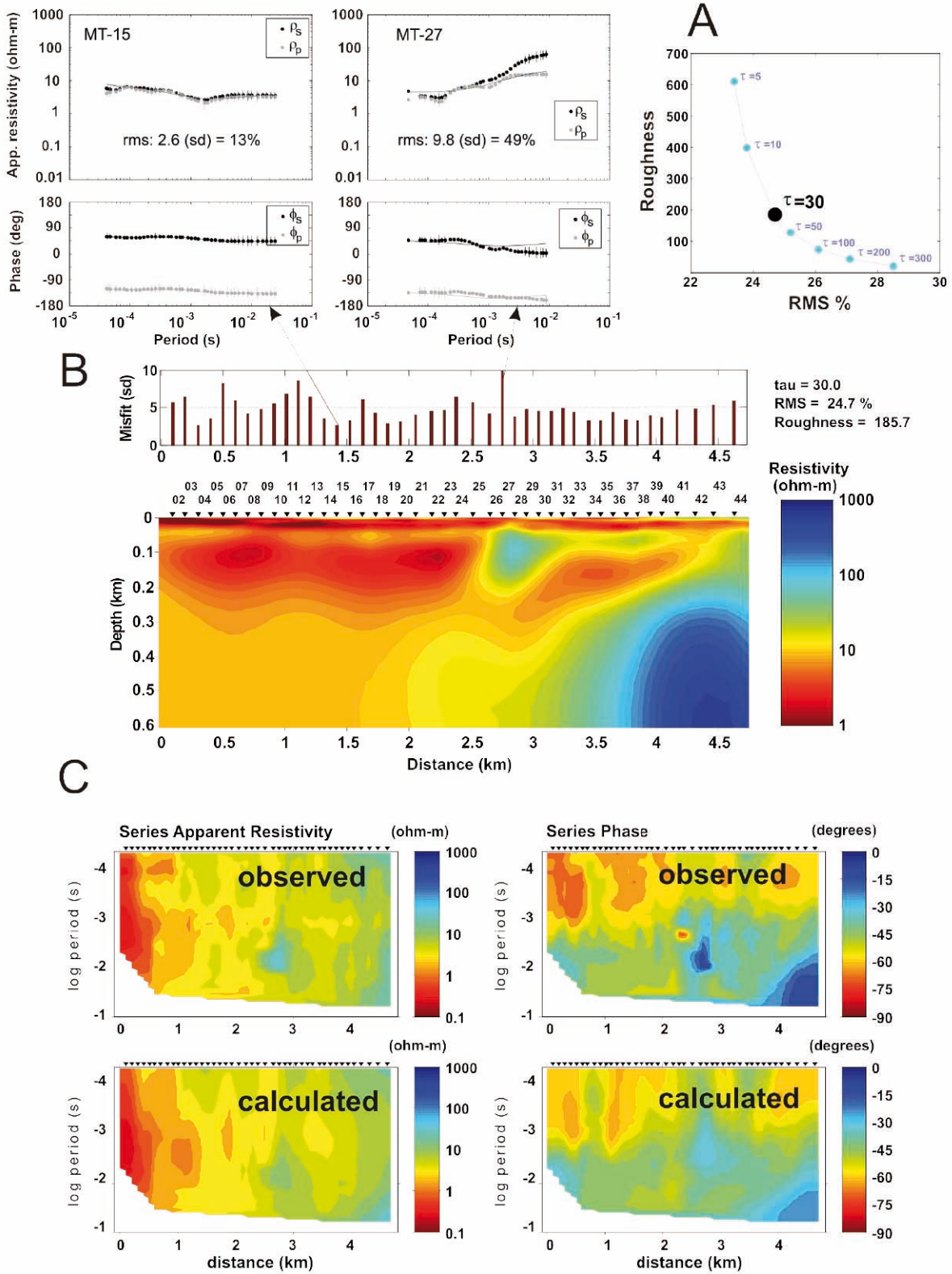


FIGURE 5 | Inversion results for Profile 3. A) L-curve showing the tradeoff between data misfit (RMS) and model roughness. The best tradeoff is for a regularization factor $\tau = 30$. B) 2-D resistivity model. The location of the AMT sites is shown by triangles at the top of the model. In the upper panel, the misfit for each individual site is shown in standard deviation (sd) units, 1 sd corresponds to an error floor of 5%. Apparent resistivity and phase curves are shown for the sites with the best and worst misfits (continuous lines correspond to model responses). C) pseudosections comparing observed and calculated responses for the series apparent resistivity and phase.

ranges from 10 to 100 ohm-m in a depth interval from 30 to 200 m. In this zone, we found several small conductive anomalies likely associated with clay lenses embedded in a sand layer. A nearby well reports sand in the shallow section followed by gravel, sand and clay in the middle, and coarse gravel at the bottom (76-100m deep). The highly resistive anomaly (> 1000 ohm-m) appearing in the middle of the profile with a horst shape may be caused by a local uplift of the granitic bedrock, as well as the high resistivity zone in the eastern end of the model below 200 m depth. The granitic rocks composing the bedrock of the basin outcrop at the eastern edge of the valley. Pérez-Flores et al. (2004) estimated the depth of the bedrock from gravity and magnetic data, their results are shown in Fig. 7. The horst and graben structures that are imaged in the resistivity model are not evident in this basement map. A possible explanation might be a lack of resolution in the gravity and

magnetic data. Alternatively, the lack of resolution might be in the AMT data themselves, as measured sites are more sparsely spaced between kilometers 3 and 4 of the horizontal distance.

The resistivity model for Profile 2 has a fairly homogeneous aspect, with medium range resistivity values (100 to 300 ohm-m), which are appreciably larger than the values found in the northern and southern profiles. This is possibly caused by a significant porosity reduction in the alluvial fan sediments deposited by a local stream, and/or by an improvement of the water quality in the zone. Below 200 m deep, the middle section of the model shows three zones with low resistivity values (~30 ohm-m) likely associated with greater porosities or higher clay content. The high resistivity zone (~1000 ohm-m) in the eastern edge of the profile is associated with basement rocks in

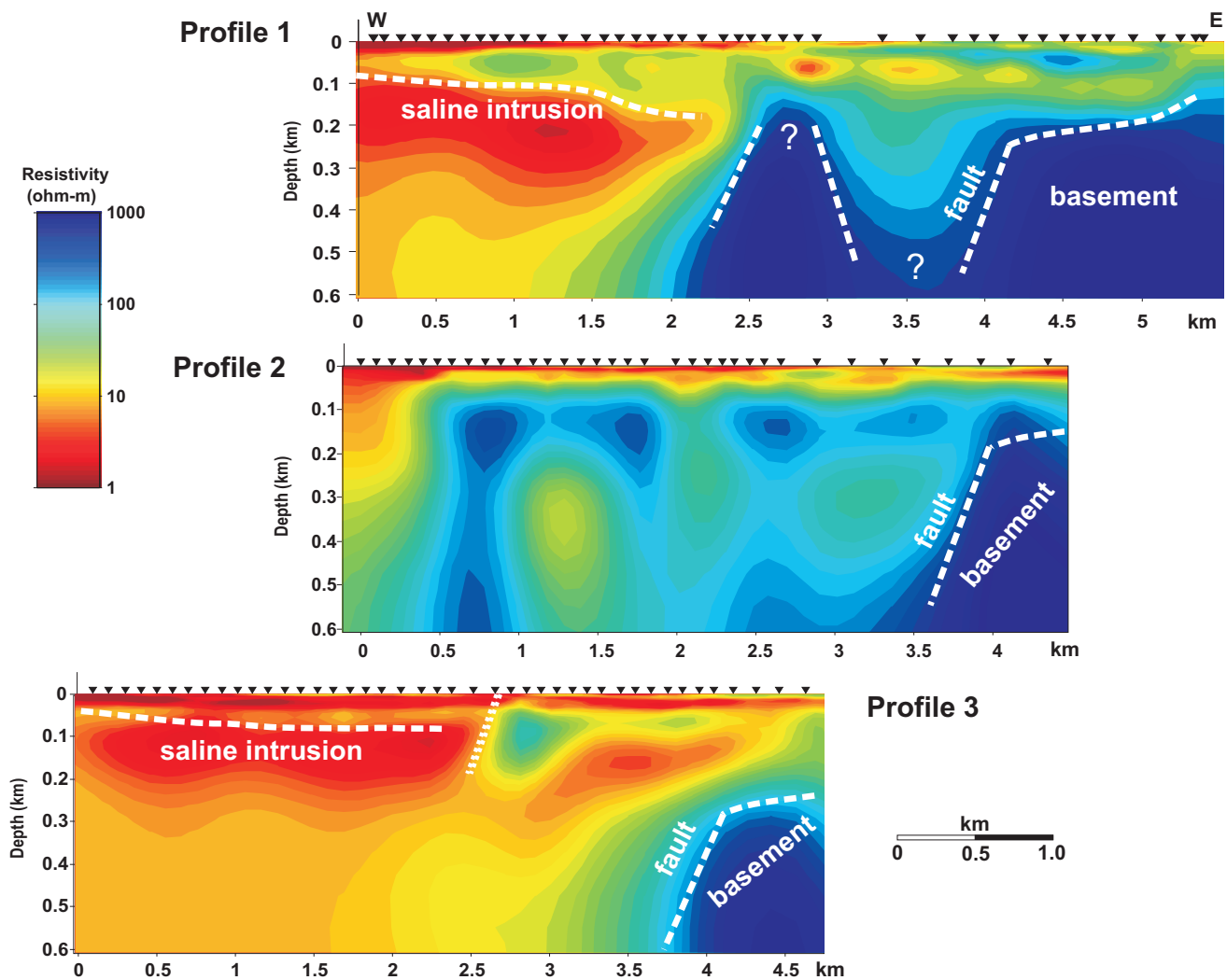


FIGURE 6 | 2-D resistivity models for the three studied profiles. The interpretation of the resistivity anomalies is indicated by the annotations.

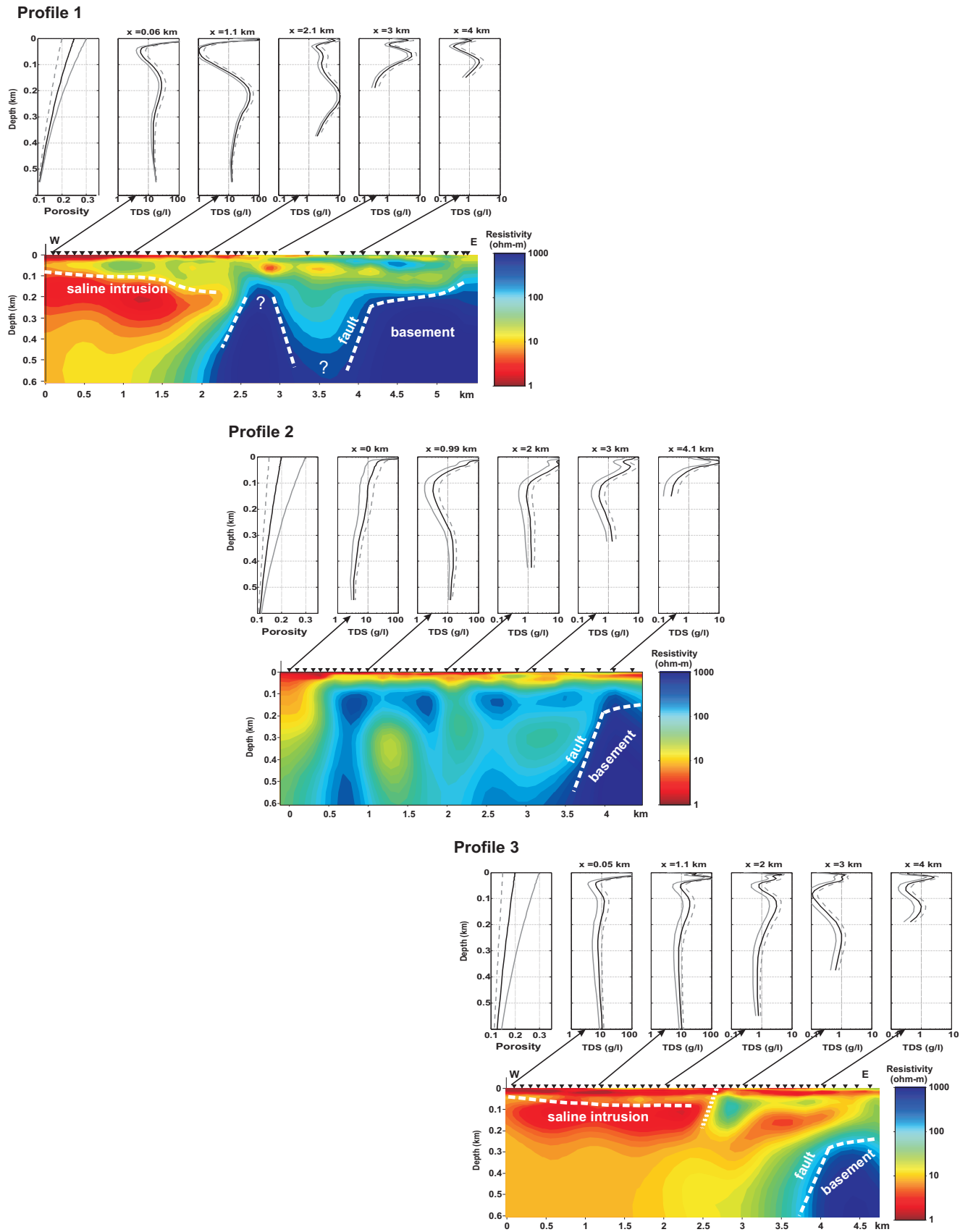


FIGURE 8 | TDS variation estimated in several points along A) Profile 1, B) Profile 2, and C) Profile 3. Estimations based on Archie's law using the resistivity model and the porosity variation shown in the upper panel.

models, we attempted to gain insights about porosity and TDS distributions in the studied area.

As Archie's law was originally derived for clay-free sedimentary rocks, the effect of clay minerals in an aquifer media must be considered. Following McNeill (1990), the clay effect in the rock conductivity can be accounted for by adding a term "in-parallel" to Archie's law, i.e.,

$$\sigma_r = \frac{1}{a} \sigma_f \phi^m + \sigma_{clay}, \quad (7)$$

where σ_r = rock conductivity

σ_f = fluid conductivity

σ_{clay} = surface conductivity caused by clay

ϕ = porosity

a, m = texture and cementation factors.

Thus, the clay effect is particularly important in fresh-water aquifers, as the presence of clay minerals provides alternative paths for electric current flow, sometimes overriding the pore-fluid ionic conductivity. As the water salinity increases, the clay-effect decreases because the pore-fluid conductivity is high enough to become the most significant term in equation (7). This equation predicts that for a given porosity of 20%, a high content of clay might reduce the rock resistivity from 60 to 10 ohm-m in a fresh-water aquifer (TDS = 1 g/l). In contrast, with a TDS = 10 g/l and the same porosity, the rock resistivity reduction is marginal, from 7 to 4 ohm-m. Equation (7) also shows that the clay-effect increases as the porosity value decreases, though this is not as significant as the salinity dependence. The TDS values reported in the studied area are in the range from 3 to 12 g/l (Daessle et al., 2004) while the presence of clay is not significantly high, as shown in the lithology description of some wells (Sarmiento-López, 1996). Hence, although it was accounted for, the clay-effect did not play an important role in our estimations. In addition, Vega-Aguilar (1989) observed low chargeability values in this area using the induced polarization method, which indicates that the clay content is fairly low.

Thus, utilizing Archie's law, we estimate the pore-fluid resistivity considering different variations of porosity with depth. The porosity variation range close to the surface was constrained to predict the TDS values measured in shallow wells by Daessle et al. (2004). The pore-fluid resistivity was then used to estimate the TDS content with the linear relationship described by Keller (1987). The analysis was made at several sites along the three modeled profiles. Fig. 8A shows the results from Profile 1. Porosity ranges between 20 and 30% in the surface and decreases exponentially to 10% at a depth of 600 m, with three different decreasing exponents. The resulting TDS vs. depth profiles are shown

for different sites along the cross-section. In the zone interpreted as seawater intrusion, the TDS values reach 40 g/l. In fact, the porosity decreasing exponents were chosen to fulfill this condition as a way to "calibrate" the TDS results in other points along the profile. As expected, TDS decreases eastward to values of 2 to 5 g/l. Since the bedrock ascends eastward, we limited the TDS calculation to depths above the basement. The calculations for Profile 2 are shown in Fig. 8B. In this profile, the resistivity distribution is fairly homogeneous and shows higher values. A larger rock resistivity can be accounted for by a low porosity or by low TDS values (higher pore-fluid resistivity). Thus, we tested a wider variation range for the exponentially decreasing porosity functions, with values between 15 and 30% at the surface, and 10% at a depth of 600 m. Even with the lower porosities, the resulting TDS values were close to 1 g/l below 100 m deep at the sites located farther than 1 km from the coast. This seems to indicate that the cause of the relatively high rock resistivity might be attributed to better quality water (TDS < 1 or 2 g/l) instead of a low porosity media. For Profile 3 (Fig. 8C), the porosity was set in the range between 15 and 30% near the surface, with an exponential decrease to 10% at 600 m depth. The TDS profiles show values greater than 10 g/l associated with the zone interpreted as seawater intrusion. A striking change can be observed in the TDS profile corresponding to the point where a shallow resistive anomaly was interpreted as an impermeable barrier. In this case, the cause of the rock resistivity increment might be a dramatic reduction in porosity. Hence, the resulting TDS profile is invalid since no local porosity changes were accounted for in our calculations. The rest of the points along the profile show relatively high TDS values in agreement with the salt content measured by Daessle et al. (2004) in shallow wells located in the vicinity.

CONCLUSIONS

Joint inversion of the s-p impedances produced consistent resistivity models that reasonably account for the underground resistivity distribution in the studied area. Our results provide original information about the extension of seawater intrusion in the aquifer. In addition, porosity and TDS values estimated with the resistivity model information are in good agreement with the expected porosity values and TDS observations in the aquifer. Porosity values between 15 and 25% near the surface reasonably predict the TDS values observed in several shallow wells located in the area (Daessle et al., 2004). TDS values range from 40 g/l (typical of seawater) to 1 g/l in the eastern edge of the basin, 4 km away from the coastline. The best conditions for the aquifer were found in Profile 2, where the resistivity model predicts TDS values close to 1 g/l below 100 m depth at sites located farther than 1 km from the coast.

Given the relatively simple geometry of the studied area, TE-TM impedances obtained from conventional decomposition methods might give models as plausible as the ones obtained here with the s-p invariant impedances. However, we found several benefits of using s-p invariant impedances: 1) their calculation from the measured tensor is straightforward; 2) they do not depend on the reference axes, therefore no rotation is needed, 3) like TE-TM modes, they form a pair of complementary responses sensible to both, galvanic and inductive effects. The cost to pay for these benefits is a loss of lateral sensitivity, although not as great as that corresponding to the use of the determinant of the impedance tensor.

ACKNOWLEDGMENTS

The authors are grateful to two anonymous reviewers as well as to Enrique Gómez-Treviño for their valuable suggestions to improve this paper. We thank the personnel of the Applied Geophysics department of CICESE who participated in the field work. We are particularly grateful to Angel Daniel Peralta, Jaime Calderón, Alejandro Díaz, Almendra Villela and Ricardo Antonio-Carpio. This project was supported with funds provided by the Secretaría del Medio Ambiente Recursos Naturales y Ecología (SEMARNAT) as well as by Consejo Nacional de Ciencia y Tecnología (CONACYT), FOSEMARNAT-2004-01-312. We are also grateful to CONACYT for the scholarship grant to Violeta Luján, who obtained her Master in Sciences degree with this work.

REFERENCES

- Abbott, P.L., Suárez-Vidal, F., Sanguines, E.M., Rendina, M.A., 1993. South Coastal Geological Society Baja California field-trip road log. In: Abbott, P.L., Sanguines, E.M., Rendina, M.A. (eds.). *Geologic investigations in Baja California, México*. Santa Ana, C.A. (USA), Annual field-trip guide book n° 21: South Coast Geological Society, Inc., 194-216.
- Archie, G.E., 1942. The electrical resistivity log as an aid in determining some reservoir characteristics. *Petroleum Technology*, 1, 55-67.
- Bahr, K., 1988. Interpretation of the magnetotelluric impedance tensor: regional induction and local telluric distortion. *Journal of Geophysics*, 62, 119-127.
- Bahr, K., 1991. Geological noise in magnetotelluric data: A classification of distortion types. *Physics of the Earth and Planetary Interiors*, 66, 24-38.
- Cruz-Castillo, M., Delgado-Argote, L.A., 2000. Los deslizamientos de la carretera de cuota Tijuana-Ensenada, Baja California. *Geos*, 20, 418-432.
- Cruz-Falcón, A., 1986. *Gravimetría de la cuenca del arroyo San Carlos, Ensenada, Baja California*. Doctoral Thesis. Ensenada, CICESE, 82pp.
- Daessle, W., Sánchez, E.C., Camacho-Ibar, V.F., Mendoza-Espinoza, L.G., Carriquiry, J.D., Macias, V.A., Castro, P.G., 2004. Geochemical evolution of groundwater in the Maneadero coastal aquifer during a dry year in Baja California, México. *Hydrogeology Journal*, 13, 584-595.
- Eggers, D.E., 1982. An eigenstate formulation of the magnetotelluric impedance tensor. *Geophysics*, 47, 1204-1214.
- Fabriol, H., Martínez, M., Vázquez, R., 1982. Mediciones gravimétricas y telúricas en el Valle de Maneadero, Ensenada, Baja California. *Geofísica Internacional*, 21, 41-55.
- Farquharson, C.G., Oldenburg, D.W., 2004. A comparison of automatic techniques for estimating the regularization parameter in non-linear inverse problems. *Geophysical Journal International*, 156, 411-425.
- Gastil, R.G., Phillips, R.P., Allison, E.C., 1975. *Reconnaissance geology of the State of Baja California*. The Geological Society of America, 140, 170pp.
- Giroux, B., Chouteau, M., Descloitres, M., Ritz, M., 1997. Use of the magnetotelluric method in the study of the deep Maestrichtian aquifer in Senegal. *Journal of Applied Geophysics*, 38, 77-96.
- Groom, R.W., Bailey, R.C., 1989. Decomposition of magnetotelluric impedance tensors in the presence of three-dimensional galvanic distortion. *Journal of Geophysical Research*, 94B, 1913-1926.
- Groom, R.W., Bailey, R.C., 1991. Analytic investigations of the effects of near-surface three-dimensional galvanic scatterers on MT tensor decompositions. *Geophysics*, 56, 496-518.
- Hansen, C., 1992. Analysis of Discrete Ill-Posed Problems by Means of the L-Curve. *SIAM Review*, 34(4), 561-580.
- Keller, G.V., 1987. Rock and mineral properties. In: Nabighian, M.N. (ed.). *Electromagnetic methods in applied geophysics: Theory*. Tulsa (Oklahoma), Society of Exploration Geophysicists, 1, 1-135.
- Kirsch, R., 2006. *Groundwater Geophysics: A Tool for Hydrogeology*. Springer, 493pp.
- McNeill, J.D., 1990. Use of electromagnetic methods for groundwater studies. In: Ward, S.H. (ed.). *Geotechnical and Environmental Geophysics. Review and Tutorial*. Tulsa (Oklahoma), Society of Exploration Geophysicists, 1, 191-211.
- Meju, M.A., Fontes, S.L., Oliveira, M.F.B., Lima, J.P.R., Ulugergerli, E.U., Carrasquilla, A.A., 1999. Regional aquifer mapping using combined VES-TEM-AMT/EMAP methods in the semiarid eastern margin of Parnaíba Basin, Brazil. *Geophysics*, 64(2), 337-356.
- Pérez-Flores, M., Suárez-Vidal, F., Gallardo-Delgado, A., González-Fernández, A., Vázquez, R., 2004. Patrón Estructural de la Planicie Costera de Todos los Santos, con base de datos geofísicos. *Ciencias Marinas*, 30, 349-364.
- Ritz, M., Descloitres, M., Robineau, B., Courteaud, M., 1997. Audiomagnetotelluric prospecting for groundwater in the Baril coastal area, Piton de la Fournaise Volcano, Reunion Island. *Geophysics*, 62, 758-762.
- Rodi, W., Mackie, R.L., 2001. Nonlinear conjugate gradients algorithm for 2D magnetotelluric inversion. *Geophysics*, 66, 174-187.

- Romo, J.M., Gómez-Treviño, E., Esparza, F.J., 2005. Series and parallel transformations of the magnetotelluric impedance tensor: theory and applications. *Physics of the Earth and Planetary Interiors*, 150, 63-83.
- Sarmiento-López, C., 1996. Modelo preliminar de Flujo tridimensional del acuífero de la planicie costera del Valle de Maneadero, B.C, México. Doctoral Thesis. Ensenada, CICESE, 157pp.
- Suárez-Vidal, F., 2006. Depositional environment of the late Cretaceous Rosario Formation in the Peninsula Punta Banda, Ensenada, Baja California, México. In: Girty, G. (ed.). Using stratigraphy, sedimentology, and geochemistry to unravel the geologic history of the southwestern cordillera. *Society for Sedimentary Geology*, 111-122.
- Suárez-Vidal, F., Armijo, R., Morgan, G., Bodin, P., Gastil, R.G., 1991. Framework of recent and active faulting in northern Baja California. In: Dauphin, J.P., Simoneit, B., (eds.). *The gulf and peninsular province of the Californias*. Tulsa (Oklahoma), American Association of Petroleum Geologists, 47, 285-300.
- Vázquez, R., 1980. Estudio de métodos potenciales con aplicación a geohidrología del valle de Mandadero, Baja California. Doctoral Thesis. Ensenada, CICESE, 108pp.
- Vega-Aguilar, M., 1989. Combinación de sondeos de resistividad y polarización inducida en estudio de un acuífero costero. Doctoral Thesis. Ensenada, CICESE, 67pp.
- Vozoff, K., 1991. The magnetotelluric method. In: Nabighian, M.N. (ed.). *Electromagnetic methods in applied geophysics*. Tulsa (Oklahoma), Society of Exploration Geophysicists, Applications, 2(B), 641-711.
- Wilson, S.R., Ingham, M., McConchie, J.A., 2006. The applicability of earth resistivity methods for saline interface definition. *Journal of Hydrogeology*, 316(1), 301-312.
- Yee, E., Paulson, K.V., 1987. The canonical decomposition and its relationship to other forms of magnetotelluric impedance tensor analysis. *Geophysical Journal*, 61, 173-189.

Manuscript received April 2007;
revision accepted December 2008;
published Online November 2009.